


## Phase-field model for diffusion-induced grain boundary migration: An application to battery electrodes

Ananya Renuka Balakrishna, Yet-Ming Chiang, and W. Craig Carter\*

*Department of Materials Science and Engineering, Massachusetts Institute of Technology Cambridge, Massachusetts 02139, USA*

 (Received 17 June 2018; revised manuscript received 22 April 2019; published 25 June 2019)

Diffusion-induced grain boundary migration is a phenomenon in which a grain boundary moves in response to the driving forces generated by diffusing solute species. For example, diffusing solute species change the atomic volume in the host material, either by filling a vacancy with a misfitting solute atom or by expanding host lattices through interstitial diffusion. These volume changes are inhomogeneous and are stored as elastic energy in the material that drives grain boundaries. In this paper, we introduce our previously developed Cahn-Hilliard–phase-field-crystal model (CH-PFC) as a computational tool to investigate diffusion-induced grain boundary migration in crystalline materials. This multiscale phase-field model couples the composition field of a diffusing species with the crystallographic texture of a host material. We apply the CH-PFC model to battery electrodes and investigate whether interstitial solute diffusion induces grain growth in  $\text{FePO}_4/\text{LiFePO}_4$  electrodes. To this end, we compute grain growth in 60  $\text{FePO}_4$  electrodes by conducting two parallel trials: In the first trial, we cycle the electrode and calculate diffusion-induced grain growth. In the second trial, we do not cycle the electrode and calculate curvature-driven grain growth. We find a statistically significant grain growth in the cycled electrodes and negligible grain growth in the noncycled electrodes. Overall, we show that the CH-PFC model not only predicts electrode microstructures as a function of the Li composition, but also predicts the crystallographic features of an electrode during battery operation.

DOI: [10.1103/PhysRevMaterials.3.065404](https://doi.org/10.1103/PhysRevMaterials.3.065404)

### I. INTRODUCTION

Grain boundaries are two-dimensional (2D) crystallographic defects in a solid material that affect the material's mechanical, electrical, and thermal properties. For example, grain boundaries typically disrupt dislocation motion and make the material harder to deform [1]. Grain boundaries are also preferential sites for precipitation and cavitation that lead to intercrystalline fracture [2]. Furthermore, the grain size of a material alters its properties, such as the fracture toughness and hardness [3,4]. An approach, therefore, to engineering material properties would be to control its microstructural features, such as grain size and grain boundary migration, during production processes and device operation.

A grain boundary moves in response to the driving forces acting on the boundary. These driving forces include curvature [5], temperature gradients [6], residual stresses, and/or phase transformations [7]. In this paper, we focus on diffusion-induced grain boundary migration (DIGM) in crystalline materials. In these phenomena the grain boundary moves in response to the driving forces generated by a diffusing solute species [8]. For example, in certain polycrystalline materials lattice parameters vary as a function of the diffusing solute composition.<sup>1</sup> This results in lattice parameter gradients that contribute to coherency strains in the material [9]. However, the material's compliance constrains these coherency strains

and produces internal stresses. When these stresses act at grain boundaries they may induce grain boundary migration, which reduces the elastic energy of the material system [10].

We investigate the DIGM phenomenon using the lattice parameters of  $\text{FePO}_4/\text{LiFePO}_4$  battery material as an example. During charging/discharging of a battery, Li diffuses into the interstitial lattice site of intercalation (insertion-type) electrodes [11] and induces lattice volume changes of up to  $\sim 10\%$  [12]. These lattice volume changes are often anisotropic and generate coherency strains between the lithiated and the delithiated phases of the electrode [13,14] (see Fig. 1). We hypothesize that these diffusion-induced coherency strains are constrained by the electrode material's compliance and act as a driving force for grain boundary migration in polycrystalline electrodes [9,10]. We test this hypothesis in a theoretical and computational framework.

Current material models work at different length and time scales [9,15–24]. Continuum methods (such as phase-field models) typically describe the time evolution of microstructures by homogenizing the crystallographic texture of the material [15,19,25–27]. A crystallographic phase-field model builds on the classic phase-field model by introducing grain orientation as an additional order parameter [28], however, these methods do not model individual lattice distortions. Furthermore, the position and orientation of grain boundaries and edge dislocations are typically predefined in the model [28]. Atomistic models, such as first-principle methods and molecular dynamics models [20,29,30], provide atomistic insights into lattice distortions [23,31]. These approaches are not currently applicable to the length scale and time scales for microstructural evolution. Accelerated molecular dynamics

\*ccarter@mit.edu

<sup>1</sup>The lattice parameter changes typically arise from misfitting solute atoms and/or interstitial diffusion.

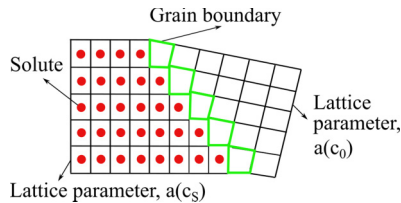


FIG. 1. Schematic of interstitial solute diffusion into a polycrystalline material. Here, the lattice parameters of the material vary with the solute concentration [i.e.,  $a(c_s)$  and  $a(c_0)$  in the presence/absence of an interstitial solute]. This gradient in the lattice parameter produces stresses at the proximity of a grain boundary that induces its movement.

methods use the transition-state theory to overcome the time-scale limitation [32] and have been applied to simulate crystal growth [33].

In our recent work [34], we combined a Cahn-Hilliard model with a phase-field-crystal model (CH-PFC). In this 2D theoretical framework, the phase-field-crystal equation models the crystallographic texture (coarse-grained lattice arrangements) of a host material, and the Cahn-Hilliard equation models the composition field of an interstitially diffusing solute species (continuum scale). The two equations are combined to describe lattice parameter changes of the host material as a function of the composition field. This coupled approach enables us to investigate whether diffusion induces grain boundary migration in the host material. We use the physical parameters of  $\text{FePO}_4/\text{LiFePO}_4$  electrodes and investigate whether interstitial diffusion induces grain growth in electrodes.

The aim of the present work is to investigate diffusion-induced grain boundary migration using the CH-PFC model as a computational tool. We first provide an overview of the CH-PFC framework using lattice parameters of  $\text{FePO}_4/\text{LiFePO}_4$  as an example. Next, we apply the model to compute diffusion-induced grain boundary migration in an  $\text{FePO}_4$  electrode during a typical charge/discharge cycle. We then test the hypothesis that interstitial solute diffusion induces grain growth in polycrystalline electrodes. We compute grain growth in 60  $\text{FePO}_4$  electrode particles each having a unique crystallographic texture in the initial state. We then randomly select these electrodes to be either cycled or not cycled. In the cycled case, we lithiate and delithiate electrodes and compute the electrode's mean grain size before and after cycling. We use the noncycled electrodes as the control set. If Li diffusion induces grain growth, then electrodes in the cycled case should demonstrate increased grain growth relative to electrodes in the noncycled case. Finally, we demonstrate DIGM by showing that grain growth in cycled electrodes is statistically greater than grain growth in noncycled electrodes.

## II. CAHN-HILLIARD-PHASE-FIELD-CRYSTAL MODEL

The CH-PFC model couples the interaction between a material's crystallographic texture and a continuum solute-composition field. This modeling approach combines two order parameters: the first is the peak density field  $\psi(\vec{x})$  (described by the phase-field-crystal equation [35]), which

represents the crystallographic texture of a host material; the second is the solute-composition field  $c(\vec{x})$  (described by the Cahn-Hilliard equation). We use the physical parameters of  $\text{FePO}_4/\text{LiFePO}_4$  to model lattices in the host material  $\psi(\vec{x})$ , and the solute-composition field  $c(\vec{x})$  represents the fraction of interstitial sites in the  $\text{FePO}_4$  electrode occupied by Li per unit volume. These two order parameters are coupled to model  $\text{FePO}_4/\text{LiFePO}_4$  lattice transformations during battery operation. Below we describe the free energy of the coupled CH-PFC model. Further details of the CH-PFC model are given in Ref. [34] and in the Appendix.

The free energy of the coupled CH-PFC model is

$$\mathcal{F} = \int \left\{ g(c) + |\nabla c|^2 + \gamma \left[ f(r, \psi) + \frac{\psi}{2} G(\nabla_c^2) \psi \right] \right\} d\vec{x}. \quad (1)$$

In Eq. (1), the polynomial  $g(c)$  represents a regular solution model [19,36] that describes a double-well potential. The two minima of this double well,  $c(\vec{x}) = 0$  and  $c(\vec{x}) = 1$ , correspond to the delithiated ( $\text{FePO}_4$ ) and lithiated ( $\text{LiFePO}_4$ ) phases, respectively.<sup>2</sup> The gradient term  $|\nabla c|^2$  is the penalty for the changing Li-composition field across the  $\text{FePO}_4/\text{LiFePO}_4$  diffuse phase boundary.<sup>3</sup> The polynomial  $f(r, \psi) + \frac{\psi}{2} G(\nabla_c^2) \psi$  is the simplest approximation of the phase-field-crystal equation that produces periodic structures. For example, in an  $\text{FePO}_4$  electrode the phase-field-crystal equation produces its coarse-grained lattice arrangements. The term  $\frac{\psi}{2} G(\nabla_c^2) \psi$  is the energy penalty resulting from the changing host-lattice structure across the diffuse phase boundary. The difference in lattice geometries between the  $\text{FePO}_4/\text{LiFePO}_4$  phases gives rise to a coherency strain across the phase boundary. This is a natural outcome from the simulation and is not modeled as an approximation from the composition field [19,37–39]. Further details of the coefficients in Eq. (1) are given in the Appendix and in Ref. [34]. Next, we give an overview of the Laplace operator  $\nabla_c^2$  and the field  $r(\vec{x})$  and describe how the CH-PFC model is solved.

The Laplace operator  $\nabla_c^2$  introduces the coupling between the electrode lattice geometry and the solute-composition field [34]. The transformation coefficients of the anisotropic Laplace operator comprise two independent variables,  $\alpha$  and  $\beta$ , which control the  $\text{FePO}_4/\text{LiFePO}_4$  lattice geometries.<sup>4</sup> These variables are functions of the composition field,  $\alpha(c) = \alpha_{\text{FP}} + (\alpha_{\text{LFP}} - \alpha_{\text{FP}})c$  and  $\beta(c) = \beta_{\text{FP}} + (\beta_{\text{LFP}} - \beta_{\text{FP}})c$ , and model the  $\text{FePO}_4/\text{LiFePO}_4$  lattice symmetries. For example, with Li composition  $c(\vec{x}) = 0$  and  $c(\vec{x}) = 1$ , the transformation coefficients correspond, respectively, to the lattice geometries of  $\text{FePO}_4$  and  $\text{LiFePO}_4$  in the  $a$ - $c$  (or  $a_1$ - $a_3$ ) plane (see Table I). Across a diffuse interface, where

<sup>2</sup>The  $X$  in  $\text{Li}_X\text{FePO}_4$  and  $c(\vec{x})$  are related by normalization coefficients that rescale the double-well potential described by  $g(c)$ .

<sup>3</sup>The  $\text{FePO}_4/\text{LiFePO}_4$  phase transition is first order, however, an interphase region  $\text{Li}_X\text{FePO}_4$  with  $0 < X < 1$  has been observed in experiments [40,44]. This interphase region reduces lattice misfit at  $\text{FePO}_4/\text{LiFePO}_4$  contact [44]. In the present work, we approximate the interphase region to correspond to a diffuse phase boundary.

<sup>4</sup>Both  $\text{FePO}_4$  and  $\text{LiFePO}_4$  have orthorhombic symmetries and undergo displacive transformations as a function of the Li composition.

TABLE I. List of lattice parameters ( $a_1$ ,  $a_3$ ) for FePO<sub>4</sub> and LiFePO<sub>4</sub> used in CH-PFC simulations [41]. The variables  $\alpha$  and  $\beta$  are calculated using  $a_0 = a_{3(\text{FePO}_4)} = 4.788 \text{ \AA}$  as the reference. These coefficients describe rectangular geometries of FePO<sub>4</sub> and LiFePO<sub>4</sub> lattices at  $c = 0$  and  $c = 1$ , respectively.

	$a_1$ (Å)	$a_3$ (Å)	$\alpha = \frac{a_1}{a_0}$	$\beta = \frac{a_3}{a_0}$
FePO <sub>4</sub> (FP)	9.821	$a_0 = 4.788$	2.0512	1
LiFePO <sub>4</sub> (LFP)	10.334	4.693	2.1583	0.9802

$0 < c(\vec{x}) < 1$ , the transformation coefficients are interpolated as  $\alpha(c(\vec{x}))$  and  $\beta(c(\vec{x}))$ , and averaged lattice geometries intermediate to FePO<sub>4</sub> and LiFePO<sub>4</sub> lattices are modeled.

Next, the value of the field  $r(\vec{x})$  controls the crystalline-to-amorphous transition of the peak density field. For example, with  $r(\vec{x}) = -0.2$ ,  $\psi(\vec{x})$  is a constant and Eq. (1) models a disordered/amorphous state; for  $r(\vec{x}) = +0.2$ ,  $\psi(\vec{x})$  has a periodic waveform solution that describes a crystalline state. In earlier PFC models,  $r(\vec{x})$  has been used as an approximation of the temperature gradient between ordered (solid) and disordered (liquid) phases [42,43]. In this work, we use  $r(\vec{x})$  as a proxy to model the crystalline (electrode) and amorphous (Li-reservoir) system.

Finally, the evolution of the two order parameters follows, respectively, the Cahn-Hilliard equation for interstitial solute diffusion,

$$\frac{\partial c}{\partial \tau} = \nabla^2 \frac{\delta \mathcal{F}}{\delta c}, \quad (2)$$

and the elastic-relaxation equation for the host lattice structure,

$$\frac{\partial \psi}{\partial n} = -\frac{\delta \mathcal{F}}{\delta \psi} + \frac{1}{L^2} \int \frac{\delta \mathcal{F}}{\delta \psi} d\vec{x}. \quad (3)$$

We assume that the elastic relaxation [equilibrating the peak density field in Eq. (3)] is infinitely faster than the evolution of the composition field. Consequently, we model the equilibrium lattice arrangements by maintaining  $\frac{\delta \mathcal{F}}{\delta \psi} \approx 0$  throughout the phase transition. The CH-PFC model is solved using an Euler discretization scheme in a 2D finite-difference framework. The computational grids have spacings of  $\delta x = \delta y = \frac{4\pi}{q_0 6\sqrt{3}}$  and have periodic boundary conditions.<sup>5</sup> At each grid point, the values of the composition field  $c(\vec{x})$ , the peak density field  $\psi(\vec{x})$ , and the constant  $r(\vec{x})$  are represented in discrete form as  $c_{ij}$ ,  $\psi_{ij}$ , and  $r_{ij}$ , respectively. Next, we present a CH-PFC simulation of a representative electrode and discuss its key features.

### III. APPLICATION TO ELECTRODE MICROSTRUCTURES

We model a polycrystalline FePO<sub>4</sub> electrode<sup>6</sup> surrounded by an amorphous Li reservoir using CH-PFC methods. We first describe the electrode's key features and highlight its crystallographic defects. We then track the evolution of these

crystallographic defects in two parallel studies: first, we cycle the electrode by inserting and extracting Li; second, we do not cycle the electrode and compute its peak density field evolution [i.e., Eq. (3)]. Throughout this section, we apply the CH-PFC model to a Li-storage electrode and discuss its advantages and limiting conditions. We compare the CH-PFC results with results in the existing literature on microstructures in electrode materials.

#### A. Interpreting a CH-PFC simulation

A partially lithiated electrode particle is shown in Fig. 2(a). The Li-composition field  $c_{ij}$  (indicated by the color bar) highlights the FePO<sub>4</sub> and LiFePO<sub>4</sub> phases, which are separated by a diffuse phase boundary. The peak density field  $\psi_{ij}$  describes the crystallographic texture of the host electrode. Individual peaks in Fig. 2(a) have an ellipsoidal shape; this shape is an artifact of the CH-PFC model and results from the anisotropic transformation coefficients in the Laplace operator  $\nabla_c^2$  [34]. The individual peaks correspond to the coarse-grained lattice points of the host electrode and are free to undergo displacive translations.<sup>7</sup>

Figure 2(b) shows the peak density field  $\psi_{ij}$  with a periodic waveform in the electrode region, which gradually changes to a constant value in the amorphous Li reservoir. This change in  $\psi_{ij}$  results from the abrupt change in  $r_{ij}$  values modeled across the electrode-reservoir interface. The electrode-reservoir interface is associated with a surface energy contribution resulting from the difference between the crystalline-electrode and amorphous-reservoir regions. In this work, the CH-PFC model does not account for the surface energy term. This surface energy contribution is important for investigating the wetting effects on phase transitions [45,46] and will be a subject for future study.

The “peak marker image”<sup>8</sup> highlights the crystallographic features of the FePO<sub>4</sub>/LiFePO<sub>4</sub> electrode [see Fig. 2(c)]. Label “A,” indicated by the magenta crystallographic planes, marks a coherent interface. Label “B” marks three grain boundaries that intersect to form a triple junction. The dihedral angle(s) between these grain boundaries influences the migration of the grain boundary system. Label “C” indicates a high-angle grain boundary with a misorientation angle of  $> 15^\circ$  and has a chain of edge dislocations, as shown by green circles. Label “D” shows an edge dislocation defect, highlighted by a pair of short blue lines. These crystallographic features are an emergent phenomenon of the

<sup>7</sup>Note that these are not atomic sites of the electrode material and correspond to the coarse-grained lattice points [34]. In the PFC formalism, new peaks can emerge or disappear on the computation grid. However, this nonconservation of peaks does not affect the coarse-grained lattice geometry of the electrode. The width of the diffuse phase boundary is numerically calibrated to span approximately four lattice spacings, as described by  $\psi(\vec{x})$  [see box AA in Fig. 2(a)]. This phase boundary is analogous to the “staging structure” observed in some intercalation compounds with a nonstoichiometric Li composition in the interface (i.e., Li<sub>X</sub>FePO<sub>4</sub>, where  $0 < X < 1$ ) [44].

<sup>8</sup>Where the peak centroids are substituted with a 2D Gaussian distribution.

<sup>5</sup>The length scale of the CH-PFC model is  $\frac{1}{q_0}$ .

<sup>6</sup>Diameter  $d = 290\delta_0$ ; periodic grid size,  $340\delta x \times 340\delta y$ .

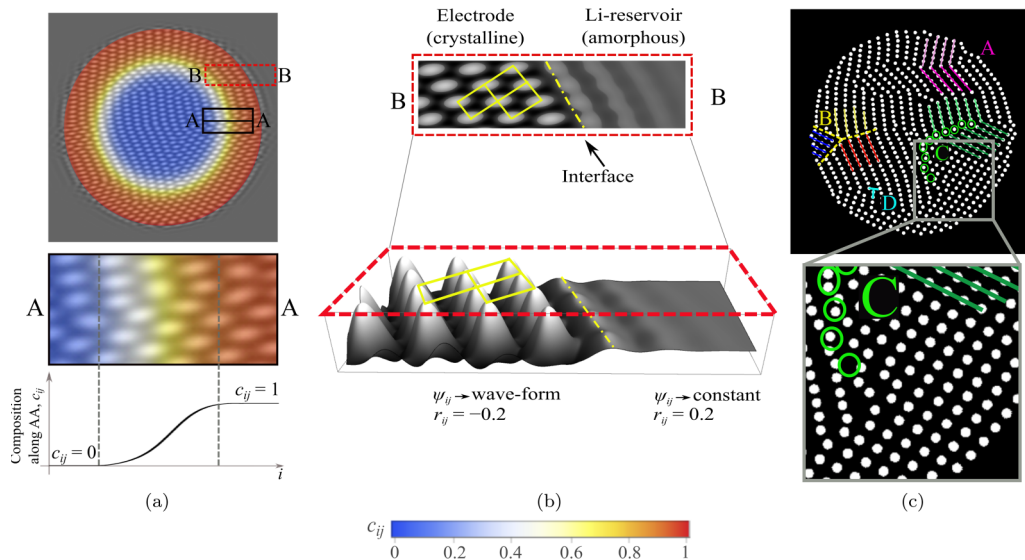


FIG. 2. (a) CH-PFC simulation of a partially lithiated  $\text{FePO}_4$  electrode particle that is surrounded by an amorphous Li reservoir. The color bar shows the Li composition in  $\text{FePO}_4$  (blue;  $c_{ij} = 0$ ) and  $\text{LiFePO}_4$  (red;  $c_{ij} = 1$ ) phases. The small black box shows a diffuse phase boundary (yellow;  $0 < c_{ij} < 1$ ) separating the two phases along AA. The width of this diffuse interface (highlighted by dashed vertical lines) is numerically calibrated to span approximately four lattice points. (b) Enlarged image of the electrode lattice symmetry is shown in the box labeled BB. In the electrode region, the peak density field  $\psi_{ij}$  has a waveform where the coordination symmetry of ellipsoidal peaks represents a  $\text{LiFePO}_4$  lattice. In the Li-reservoir region,  $\psi_{ij}$  is a constant and describes an amorphous state. At the electrode-reservoir interface,  $\psi_{ij}$  changes as a function of  $r_{ij}$  according to Eq. (A1). (c) “Peak marker image” illustrating the crystallographic features in the polycrystalline electrode: coherent interface, A; triple junction, B; chain of defects, enclosed in green circles, which forms a high-angle grain boundary ( $> 15^\circ$ ), C', and an edge-dislocation defect, D.

CH-PFC simulation [47], unlike in previous works, where these features were empirical parameters in the model [28]. We next lithiate and delithiate this electrode to investigate how its crystallographic features evolve during battery operation.

### B. Cycled electrode

To lithiate/delithiate the electrode, we specify a chemical potential to the Li reservoir that is held fixed during the computation. This boundary condition is a proxy for our assumption that the Li intercalation rate is higher in the reservoir than in the electrode particle. For example, we specify the Li reservoir with  $c_{ij} = 1$ , which is fixed during lithiation. The composition gradient between the  $\text{FePO}_4$  electrode ( $c_{ij} = 0$ ) and the Li reservoir creates a boundary condition, which causes Li to diffuse into the electrode.<sup>9</sup>

Two features of this work limit the strength of the conclusions we can draw about Li-diffusion-induced grain growth. The first limitation is the “artificial boundary condition” applied to the electrode-reservoir interface (see Fig. 3). The electrode volume (or area) is held constant during the computation, though the number density of peaks in this electrode is not conserved. Peaks move in/out at the electrode-reservoir interface to accommodate the lattice-area change during  $\text{FePO}_4/\text{LiFePO}_4$  phase transition.<sup>10</sup> This artificial boundary condition does not impose volume-confinement stresses on

the electrode, which could affect grain growth in electrode particles. The second limitation is that Li diffusion is modeled as a boundary-condition-driven diffusion, and electromigration is currently not incorporated in the CH-PFC model. A possible refinement to this model would be to solve the Poisson-Nernst-Planck equation to investigate whether treating Li as a charged particle will yield comparable results on diffusion-induced grain growth. At present, we investigate whether diffusion-induced lattice volume changes (elastic energy changes) in the electrode alone induce grain growth.

Figure 3 shows the temporal evolution of the electrode’s microstructure during battery operation. The top row shows the electrode’s lattice arrangements as a function of the Li composition. The middle row shows the approximate positions of representative grain boundaries A–D. The bottom row shows the distortion maps, which illustrate  $\text{FePO}_4/\text{LiFePO}_4$  coarse-grained lattice transformations during battery operation. In these maps, a voronoi mesh for the lattice points is generated, and the centroid of each voronoi cell is calculated.<sup>11</sup> The distortion is calculated as the absolute difference in the centroid positions with a reference state  $\delta_{ij} = \frac{\|x_{ij}(\tau) - x_{ij}(\tau=0)\|}{\delta_0}$ . The numerator represents the euclidean distance between a centroid position  $x_{ij}$  at time  $\tau$  and its

<sup>9</sup>During delithiation the Li reservoir is held fixed at  $c_{ij} = 0$  and Li diffuses out of the  $\text{LiFePO}_4$  electrode.

<sup>10</sup>Please note that the addition/removal of peaks does not affect the coarse-grained lattice structure described by  $\psi_{ij}$  [34].

<sup>11</sup>In the PFC formalism, calculating individual lattice distortions would be prone to artifacts arising from the nonconservation of peaks. We have addressed this challenge by plotting voronoi mesh, which describes the coarse-grained lattices in a polycrystalline electrode. The centroids of individual voronoi cells are then used to compute coarse-grained lattice distortions as shown in Fig. 4.

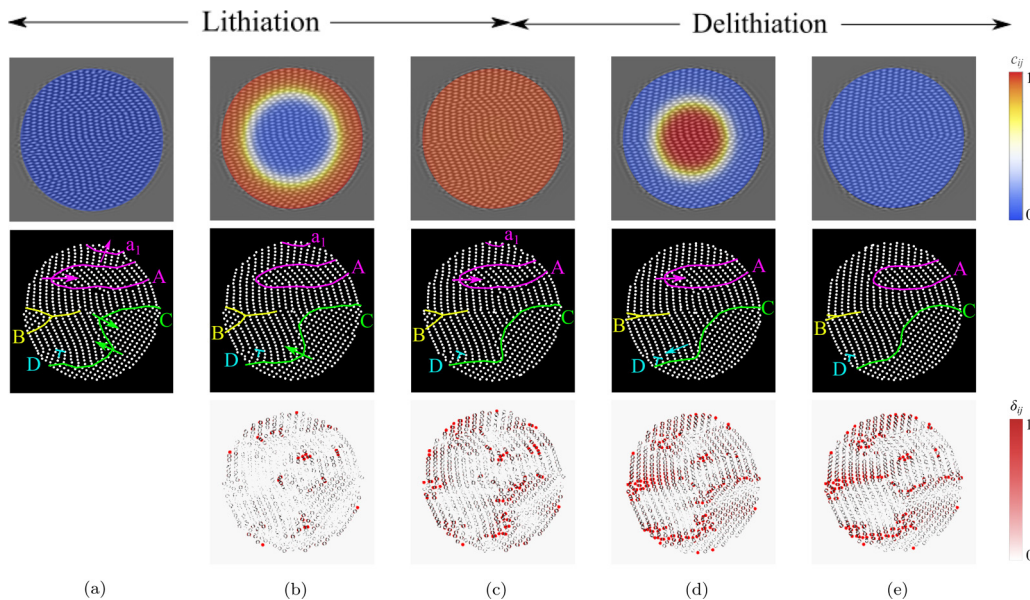


FIG. 3. Lithiation of the polycrystalline  $\text{FePO}_4$  electrode particle. Starting from an initial  $\text{FePO}_4$  phase (a), Li ions intercalate into the electrode particle (b, c). A  $\text{LiFePO}_4$  phase is formed at the end of lithiation (d). The plots in the top row show the temporal evolution of the Li composition  $c_{ij}$  in the electrode particle. The plots in the middle row show the structural transformation of lattices in the host-electrode during lithiation. Labels A–D highlight representative crystallographic features in the electrode particle. The plots in the bottom row illustrate the distortion maps  $\delta_{ij}$  corresponding to each stage of lithiation. We interpret  $\delta_{ij}$  to show coarse-grained lattice distortions induced from Li intercalation.

initial position at  $\tau = 0$  in Fig. 3(a). The normalizing constant,  $\delta_0 = \beta_{\text{FP}} = \frac{4\pi}{q_0\sqrt{3}}$ , is the equilibrium separation between two adjacent Gaussian peaks.

The CH-PFC simulations provide insights into atomistic features of electrode microstructures during battery operation. For example, grains  $a_1$  and B shrink until they disappear at the end of the lithiation/delithiation cycle (see middle row in Fig. 3). Although grains  $a_1$  and B are of comparable sizes, Fig. 3 qualitatively illustrates that grain  $a_1$  shrinks more rapidly than grain B. We interpret this slow migration of the grain boundary system B as resulting from the triple-junction drag effect. Another feature captured by these simulations is that grain boundaries such as C tend to move towards their center of curvature. This is consistent with motion by curvature observed in material microstructures [5,48,49]. The edge dislocation D is also observed to move towards the electrode particle's surface during delithiation. In these simulations we refer to the grain boundary motion with a local change in orientation that requires no long-range diffusion. The activation energy for the displacements to achieve this grain boundary motion could be related to the solute atmosphere, and therefore separation of time scales between crystallographic texture evolution and Li diffusion would be possible [48]. In our computations, we solve crystallographic texture evolution using Eq. (3), which is instantaneous in comparison to Li diffusion [Eq. (2)].

The distortion maps indicate lattice distortions  $\delta_{ij} \approx 0.12$  in the lithiated/delithiated phases of the electrode particle (see bottom row in Fig. 3). We interpret these distortions as corresponding to the lattice strains that accompany the  $\text{FePO}_4/\text{LiFePO}_4$  phase transition. We observe relatively

greater distortions  $\delta_{ij} > 0.5$  along grain boundaries in the electrode. We interpret these greater distortions as corresponding to the grain boundary migration. The distortion maps highlight a couple of advantages of the CH-PFC model. The first is that lattices deform independently as a function of the interstitial solute composition. This generates an inhomogeneous strain field in the electrode because lattice geometries differ across phases. The second is that crystallographic defects in the polycrystalline electrodes, such as grain boundaries and edge dislocations, also contribute to the inhomogeneous strain field in electrode particle.

Figure 3 shows the isotropic Li diffusion in electrodes, however, in olivine materials, such as  $\text{FePO}_4$ , Li preferentially diffuses through the host's one-dimensional channels [50]. This preferential Li intercalation is not observed in the polycrystalline electrode in Fig. 3. In previous continuum models [13,14,16,26], where the crystallographic planes of  $\text{FePO}_4$  are fixed, researchers have modeled anisotropic Li intercalation with reference to a Cartesian plane. In the CH-PFC model, however, the crystallographic planes of  $\text{FePO}_4/\text{LiFePO}_4$  emerge from simulations, and we assume an isotropic bulk-diffusion coefficient  $D$  in Eq. (2). We do, however, see anisotropy in Li diffusion because of the coordinate transformation coefficients in the coupled term  $\nabla^2 \gamma \frac{\psi}{2} \frac{\partial G(\nabla^2 \psi)}{\partial c}$  in Eqs. (1) and (2). This anisotropic effect is negligible in Fig. 3 because the diffuse phase boundary spans approximately four lattice spacings. We discuss details of this anisotropic effect further in the Appendix.

Another feature to note is that, despite the thermodynamic transition modeled by the CH-PFC model Eq. (1), none of the lamellar phase separation morphologies observed in

$\text{FePO}_4/\text{LiFePO}_4$  electrodes appear in the computations in Fig. 3. Such lamellar structures are typically derived from stored elastic energy in the system. For larger systems, the conditions for lamellar structure can be treated with continuum treatments [51]. We hypothesize that, for the smaller particles treated in this paper, the stored elastic energy is not high enough to create lamellar structures or that the external surface affects the internal morphology. We propose to explore the interaction between crystallographic features and phase separation morphologies in electrodes at larger length scales in a future study.

Overall, several features of CH-PFC simulations in Fig. 3 are consistent with the microstructural evolution observed in experiments. For example, the triple-junction drag effect has been observed by Shvindlerman *et al.* [52,53] and has also been reported for electrode microstructures [54]. Dislocation dynamics under an external load have been observed in experiments [55,56], when an applied current induced dislocation movement in an intercalation cathode particle ( $\text{LiNi}_{0.5}\text{Mn}_{1.5}\text{O}_4$ ). The dislocation was stable at room temperature and migrated to the particle surface under an electrical load [55]. Similarly, in hydrogen-palladium nanocubes hydrogen diffusion into palladium particles mobilized edge dislocations in the particle [56]. These past experimental observations are consistent with the CH-PFC computations; Fig. 3 suggests that Li intercalation affects grain boundary and edge-dislocation migration. We next explore whether grain boundaries in the electrode particle are equally mobile without Li intercalation (i.e., no additional driving force).

### C. Noncycled electrode

Starting from the same electrode as in Fig. 3(a), we model a homogeneous Li-composition field  $c_{ij} = 0$  on the computation grid. The peak density field is evolved by iterating Eq. (3) for the same time  $\tau_{\text{total}}$  as required to cycle the electrode in Fig. 3. We refer to this computation as the “noncycled grain growth” of the electrode.

Figures 4(a) and 4(b) illustrate, respectively, the lattice arrangements in the electrode before and after the computation. The lattice distortion map in Fig. 4(c) shows structural rearrangements in the electrode. Lattice distortions  $\delta_{ij} \approx 1$  are primarily observed along grain boundaries with a nonzero

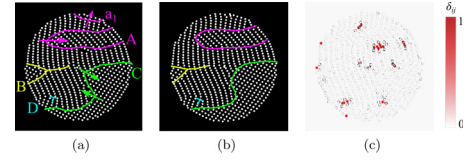


FIG. 4. Lattice rearrangements in the noncycled polycrystalline electrode particle. The electrode-reservoir system is modeled with a homogeneous Li composition  $c_{ij} = 0$  and computed for the same time ( $\tau_{\text{total}}$ ) and temperature as in Fig. 3. Host-electrode lattice arrangements (a) before,  $\tau/\tau_{\text{total}} = 0$ , and (b) after,  $\tau/\tau_{\text{total}} = 1$ , the noncycled grain growth. (c) The lattice distortion map  $\delta_{ij}$  calculated as the absolute difference in centroid positions between the before and the after stages of the noncycled electrode. The distortion map illustrates coarse-grained lattice rearrangements near grain boundaries.

radius of curvature. This suggests that curvature drives grain boundary migration in Figs. 4(b) and 4(c). These migrations are, however, small in comparison to those in Fig. 3. For example, in Fig. 3 grain B shrinks at the end of the lithiation/delithiation cycle. In Fig. 4, however, with no interstitial solute diffusion, grain B decreases in size only slightly. Similarly, grains A and C show a small variation in their shape and size. Figures 3 and 4 suggest that interstitial solute diffusion assists (or accelerates) grain boundary migration. We next test the statistical significance of this comparison by computing grain growth across 60  $\text{FePO}_4$  electrodes of two sizes.

### IV. DOES Li DIFFUSION INDUCE GRAIN GROWTH IN INTERCALATION ELECTRODES?

We compute grain growth in 60 polycrystalline  $\text{FePO}_4$  electrodes of sizes  $d = 50\delta_0$  and  $d = 100\delta_0$ . First, we choose one half of the electrodes (at random) to compute a pairwise comparison of grain growth. That is, we compute the grain size in the same electrodes both before and after electrochemical cycling (intervention-cycled set) and before and after an equivalent time of noncycling (paired-noncycled set). Second, we compute the grain size before and after an equivalent time of noncycling in the remaining half of the electrodes

TABLE II. Description of notations used in grain growth calculations.

Notation	Description
$d$	Electrode size
$g_i^0/d$	Grain size of the $i$ th electrode before CH-PFC computation normalized by electrode size (at $\tau = 0$ )
$g_i^\tau/d$	Grain size of the $i$ th electrode after CH-PFC computation normalized by electrode size (at $\tau = \tau_{\text{total}}$ )
$G_i$	Grain growth in the $i$ th electrode at the end of CH-PFC computation ( $(g_i^\tau - g_i^0)/d$ )
$G_i^{\text{IC}}, G_i^{\text{PN}}, G_i^{\text{UN}}$	Grain growth in the $i$ th electrode of the intervention-cycled (IC) set, paired-noncycled (PN) set, and unpaired-noncycled (UN) set, respectively
$\overline{\Delta G}_{\text{IC-PN}}, \overline{\Delta G}_{\text{IC-UN}}, \overline{\Delta G}_{\text{PN-UN}}$	Mean difference in grain growth between IC and PN sets $\frac{1}{n} \sum_{i=1}^n (G_i^{\text{IC}} - G_i^{\text{PN}})$ , where $n$ is the total number of electrodes in each set. Likewise, $\overline{\Delta G}_{\text{IC-UN}}$ and $\overline{\Delta G}_{\text{PN-UN}}$ are the mean differences in grain growth between intervention and unpaired sets and between paired and unpaired sets, respectively.

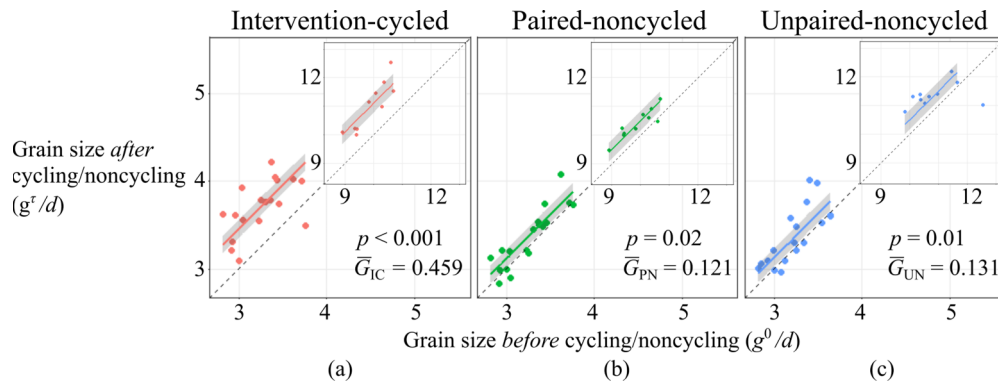


FIG. 5. Grain sizes in electrode particles  $d = 50\delta_0$  (inset:  $d = 100\delta_0$ ) in the (a) intervention-cycled, (b) paired-noncycled, and (c) unpaired-noncycled sets. Axes indicate the grain size in electrodes before ( $g^0$ ) and after ( $g^r$ ) CH-PFC computations. The dotted line is a reference line along which there is zero grain growth in electrodes. Solid lines show the linear model fit to the data points, and gray-shaded areas correspond to the 95% confidence interval. There is statistically significant grain growth in all three sets ( $p < 0.05$ ), however, the estimated mean grain growth in the intervention-cycled ( $\bar{G}_{IC} = 0.459$ ) set is greater than the estimated mean grain growth in the paired-noncycled ( $\bar{G}_{PN} = 0.121$ ) and unpaired-noncycled ( $\bar{G}_{UN} = 0.131$ ) sets.

(unpaired-noncycled set). In all sets, we measure grain growth after a computational time of  $\tau_{\text{total}}$ . Furthermore, we estimate the size of the differences in grain growth between the three sets using a linear parametric model. Comparing the intervention-cycled set to both the paired- and the unpaired-noncycled sets shows to what extent any observed effects are dependent on the specific microstructures in the paired sets. In this section, we test our hypothesis that the grain growth in intervention-cycled electrodes is greater than grain growth in both the paired-noncycled and the unpaired-noncycled electrodes. To support our hypothesis we need to satisfy two conditions: (a) the mean difference in grain growth between the cycled and the noncycled sets is statistically significant ( $p < 0.05$ ) in both the intervention-paired and the intervention-unpaired comparisons; and (b) the mean difference in grain growth between the two noncycled sets (i.e., paired-unpaired comparison) is not statistically significant ( $p > 0.05$ ).

Before we present the results we first introduce several notations that are used in the grain growth calculations listed in Table II. The average grain sizes of an electrode before and after the CH-PFC computation are given by  $g^0/d$  and  $g^r/d$ , respectively. We compute grain growth in individual electrodes as  $G_i = (g^r - g^0)/d$ . We compute the mean differences in grain growth (for example, between the intervention-cycled and the paired-noncycled set) by subtracting the mean grain growth in the intervention-cycled set from the mean grain growth in the paired-noncycled set [ $\Delta\bar{G}_{IC-PN} = (\bar{G}_{IC} - \bar{G}_{PN})$ ]. We compute these mean differences between the intervention-paired, the intervention-unpaired, and the paired-unpaired sets for electrodes of both sizes,  $d = 50\delta_0$  and  $d = 100\delta_0$ .

To test our first condition we compute the grain size in electrodes before ( $g^0$ ) and after ( $g^r$ ) electrochemical cycling (or noncycling). Figures 5(a)–5(c) show the grain sizes in electrodes from the three sets, namely, the intervention-cycled set, paired-noncycled set, and unpaired-noncycled set. The dashed line is a reference line that indicates no grain growth in electrodes [ $G = (g^r - g^0)/d = 0$ ]. Points above

this reference line indicate electrodes with positive grain growth ( $G > 0$ ), while electrodes below the reference line indicate negative grain growth ( $G < 0$ ). Figure 5 shows that there is statistically significant grain growth in all the sets ( $p < 0.05$ ).<sup>12</sup> As hypothesized, we find a greater estimated mean of grain growth in the intervention-cycled set ( $\bar{G}_{IC} = 0.459$ ) than in either the paired-noncycled set ( $\bar{G}_{PN} = 0.121$ ,  $\Delta\bar{G}_{IC-PN} = 0.337$ ) or the unpaired-noncycled set ( $\bar{G}_{UN} = 0.131$ ,  $\Delta\bar{G}_{IC-UN} = 0.328$ ) in electrodes of size  $d = 50\delta_0$ . Likewise, in electrodes of size  $d = 100\delta_0$ , we find greater grain growth in the intervention set than in either of the paired/unpaired noncycled sets ( $\bar{G}_{IC} = 1.111$ ,  $\bar{G}_{PN} = 0.506$ ,  $\bar{G}_{UN} = 0.504$ ,  $\Delta\bar{G}_{IC-PN} = 0.605$ ,  $\Delta\bar{G}_{IC-UN} = 0.607$ ). Table III lists the mean differences in grain growth for each of the six comparisons with 95% confidence intervals and  $p$  values. All of the mean differences in grain growth involving the intervention set are statistically significant as shown in Table III. We interpret these results as follows: in the paired-noncycled and unpaired-noncycled sets, the nonzero curvature of grain boundaries induces grain growth in electrodes. However, in the intervention-cycled set, Li diffusion induces grain growth in electrodes in addition to the nonzero grain boundary curvature. This additional driving force contributes to greater grain growth in the intervention-cycled set, in comparison to the paired-noncycled/unpaired-noncycled sets.

We next test our second condition, that the mean differences in grain growth between the two noncycled sets (paired and unpaired) is statistically nonsignificant. Table III reports a negligible mean difference in grain growth between the paired-noncycled and the unpaired-noncycled sets ( $\Delta\bar{G}_{PN-UN} = -0.009$  for  $d = 50\delta_0$  and  $\Delta\bar{G}_{PN-UN} = 0.001$  for  $d = 100\delta_0$ ). As hypothesized we find that the mean difference

<sup>12</sup>Note that there are two sets of  $p$  values reported in Fig. 5 and Table III, respectively. The  $p$  values shown in Fig. 5 correspond to grain growth in individual sets, and the  $p$  values listed in Table III correspond to mean differences in grain growth between sets.

TABLE III. Confidence intervals for the mean differences in grain growth across conditions. The estimates for the intervention-paired and the intervention-unpaired sets are positive,  $\overline{\Delta G} > 0$ , suggesting that a statistically significant difference in grain growth between the cycled (intervention) and the noncycled (paired/unpaired) sets is observed ( $p < 0.05$ ). The estimates for the paired-unpaired sets are  $\overline{\Delta G} \approx 0$ , indicating a negligible difference in grain growth between the two noncycled (paired-unpaired) sets of electrodes ( $p \approx 0.89$ ).

Comparison between electrode sets A and B		Electrode size ( $d$ )	Estimated mean ( $\overline{\Delta G}_{A-B}$ )	Standard error	95% confidence interval around estimated mean		$p$ value
A	B				Lower bound	Upper bound	
Intervention-cycled	Paired-noncycled	$50\delta_0$	0.337	0.0731	0.195	0.481	<0.001
Intervention-cycled	Unpaired-noncycled	$50\delta_0$	0.328	0.0731	0.185	0.472	<0.001
Paired-noncycled	Unpaired-noncycled	$50\delta_0$	-0.009	0.0731	-0.153	0.133	0.893
Intervention-cycled	Paired-noncycled	$100\delta_0$	0.605	0.238	0.138	1.07	<0.01
Intervention-cycled	Unpaired-noncycled	$100\delta_0$	0.607	0.238	0.140	1.07	<0.01
Paired-noncycled	Unpaired-noncycled	$100\delta_0$	0.001	0.231	-0.464	0.467	0.893

between the paired and the unpaired noncycled set is not significant ( $p = 0.893$  for both electrode sizes).

Our findings support the diffusion-induced grain boundary migration discussed in the works by Handwerker *et al.* [9,10]. Li diffusion induces volume changes in the host electrode. These volume changes generate coherency strains that are constrained by the compliance of the electrode material. This results in a stored elastic energy in the system that mobilizes grain boundaries and edge-dislocation defects. These results suggest that repeatedly charging/discharging a battery increases the mean grain size in electrodes. Furthermore, electrodes with a large grain size have a reduced fracture toughness in comparison to electrodes with smaller grains [57,58]. Figure 5 suggests that Li diffusion is an additional process that affects the mechanical reliability of electrodes.

We find the work of Bates *et al.* [59] on sputter-deposited thin-film cathodes to be the closest experimental comparison to the diffusion-induced grain growth effect suggested by our present work. Bates *et al.* [59] described the cathodes as undergoing grain growth during electrochemical cycling at near-ambient temperature [59]. Other related phenomena are the observations of accelerated grain growth in fluorite-structure solid electrolytes at elevated temperatures. In these solid electrolytes the electrical load has been observed to accelerate grain growth kinetics [60,61]. We suggest that systematic experimental investigation of battery electrodes after extensive cycling will reveal diffusion-induced grain growth as observed in this paper.

More generally, our study is an application of the CH-PFC methods to investigate the coupled interaction between a solute-composition field and a material's crystallographic texture. Specifically, this modeling approach has three key advantages: First, the crystallographic texture of the electrode particle is an emergent phenomenon of the CH-PFC simulations, and grain boundaries and edge-dislocation defects are not empirical parameters in the model [47]. Second, electrode lattices distort independently as a function of the Li-composition field. This generates a coherency strain across grain boundaries and phase boundaries in polycrystalline electrodes [19,37–39]. Finally, the CH-PFC method provides qualitative insights into atomistic features of elec-

trode microstructures, *in situ*, during battery operation. These features of the CH-PFC model could help us to crystallographically engineer electrodes and to enhance their physical properties.

## V. CONCLUSION

Overall, the results demonstrate that interstitial solute diffusion induces grain growth in polycrystalline materials. We demonstrated this phenomenon using the physical parameters of  $\text{FePO}_4/\text{LiFePO}_4$  electrodes as a model system. While grain growth from cyclic intercalation has not been experimentally confirmed, our study suggests that volume changes in electrodes upon Li diffusion drives grain boundary migration. Furthermore, the results provide insights into edge-dislocation movement and the triple-junction drag effect in insertion electrodes, which are consistent with microstructural evolution observed in experiments. More generally, the present work demonstrates a potential use of the Cahn-Hilliard-phase-field-crystal model to probe diffusion-induced grain boundary migration in crystalline materials. This modeling framework could be applied to investigate crystallographic features in other chemomechanically coupled problems that involve diffusion-induced phase transitions.

## ACKNOWLEDGMENTS

A.R.B. thanks Dr. Nils K. Reimer for useful discussions of the statistical analyses and acknowledges the support of the Lindemann postdoctoral fellowship. The authors are grateful for the insightful comments and suggestions of anonymous reviewers, which helped to improve the manuscript content. The authors gratefully acknowledge the support from U.S. Department of Energy, Office of Science, Grant No. DE-SC0002633 in carrying out this work.

## APPENDIX

### 1. CH-PFC model details

In this section we provide a brief explanation of the CH-PFC model. For the derivation of the CH-PFC model please refer to Ref. [34]. The CH-PFC model describes the total free



energy  $F$  as a function of the composition field  $\bar{c}$  and the peak density field  $\phi$ :

$$\begin{aligned} F &= \int \left\{ g(\bar{c}) + \kappa |\nabla \bar{c}|^2 + f(\phi) + \frac{\phi}{2} G(\nabla_c^2) \phi \right\} d\bar{\mathbf{r}} \\ &= \int \left\{ RT[\bar{c} \ln(\bar{c}) + (1 - \bar{c}) \ln(1 - \bar{c})] + \Omega \bar{c}(1 - \bar{c}) \right. \\ &\quad \left. + \kappa |\nabla \bar{c}|^2 + \frac{\phi}{2} (a \Delta T_0 + \lambda (q_0^2 + \nabla_c^2)^2) \phi + u \frac{\phi^4}{4} \right\} d\bar{\mathbf{r}}. \end{aligned} \quad (\text{A1})$$

Equation (A1) in its normalized form is

$$\begin{aligned} \mathcal{F} = \frac{F}{F_0} &= \int \left\{ g(c) + |\nabla c|^2 + f(\psi) + \frac{\psi}{2} G(\nabla_c^2) \psi \right\} d\bar{\mathbf{x}} \\ &= \int \left\{ c \ln(c) + (1 - c) \ln(1 - c) + \Omega_0 c(1 - c) + |\nabla c|^2 \right. \\ &\quad \left. + \gamma \left( \frac{\psi}{2} (r + (1 + \nabla_c^2)^2) \psi + \frac{\psi^4}{4} \right) \right\} d\bar{\mathbf{x}}, \end{aligned} \quad (\text{A2})$$

where  $c = \frac{\bar{c}_a - \bar{c}}{\bar{c}_a - \bar{c}_b}$  and  $\psi = \phi \sqrt{\frac{u}{\lambda q_0^5}}$ . The gradient energy coefficient,  $\kappa = \frac{F_0}{(\bar{c}_a - \bar{c}_b)^2} \left( \frac{16\pi\xi}{q_0\sqrt{3}} \right)^2$ , is numerically calibrated such that the width of the diffuse composition interface spans approximately four lattice spacings described by the peak density field,  $\psi$ . Note that  $\frac{1}{q_0}$  is the length scale of the CH-PFC model and  $\xi$  is the scale factor that coarse-grains lattice units. The form of Eqs. (A1) and (A2) is similar to that in the work of Renuka-Balakrishna and Carter [34], where detailed explanations of the specific terms, constants ( $\bar{c}_a$ ,  $\bar{c}_b$ ,  $\lambda$ ,  $q_0$ ,  $u$ ,  $\xi$ ), and normalizations are provided. Note that the coefficients in the regular solution model are the same as in Ref. [38]. In Eq. (A2),  $g(c)$  and  $f(\psi)$  describe the homogeneous energy contributions from the Cahn-Hilliard and phase-field-crystal equations, respectively. The composition gradient energy is given by  $|\nabla c|^2$ . The parameter  $r$  controls the second-order phase transition of the PFC model. The constant  $\gamma = \frac{\lambda^2 q_0^5}{u F_0}$  relates the free-energy normalizations of the Cahn-Hilliard and the PFC model. In this paper we set  $\gamma = 1$  and  $\xi = 1$  for computational expediency. The Cahn-Hilliard and the phase-field-crystal models are coupled via the operator  $G(\nabla_c^2) = (1 + \nabla_c^2)^2$ . The composition field is coupled to the lattice symmetry via the Laplace operator:

$$\nabla_c^2 = \xi^2 \left( (A_{11}^2 + A_{12}^2) \frac{\partial}{\partial x^2} + A_{22}^2 \frac{\partial}{\partial y^2} + 2A_{12}A_{22} \frac{\partial}{\partial x \partial y} \right). \quad (\text{A3})$$

Here,  $A_{kl}$  are the elements of the transformation matrix and are described as functions of the composition field:

$$\mathbf{A}(c) = \begin{bmatrix} \alpha(c) & \frac{-\alpha(c)}{\sqrt{3}} \\ 0 & \frac{2\beta(c)}{\sqrt{3}} \end{bmatrix}. \quad (\text{A4})$$

The transformation matrix  $\mathbf{A}(c)$  describes affine lattice transformations using the rectangular symmetry of  $\text{FePO}_4$  as reference. The transformation coefficients are given by  $\alpha(c) = \alpha_{\text{FP}} + (\alpha_{\text{LFP}} - \alpha_{\text{FP}})c$  and  $\beta(c) = \beta_{\text{FP}} + (\beta_{\text{LFP}} - \beta_{\text{FP}})c$ . The values of  $(\alpha_{\text{FP}}, \beta_{\text{FP}})$  and  $(\alpha_{\text{LFP}}, \beta_{\text{LFP}})$  correspond to  $\text{FePO}_4$

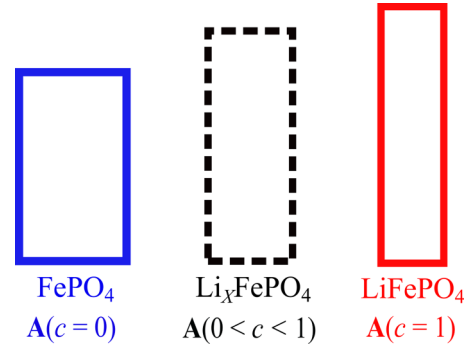


FIG. 6. Schematic of the coupling between lattice symmetry and composition field in the CH-PFC model. The transformation matrix  $\mathbf{A}(c)$  is described as a function of the composition field  $c$ . For  $c = 0$ ,  $\mathbf{A}(c)$  describes a rectangular  $\text{FePO}_4$  lattice (blue box). For  $c = 1$ ,  $\mathbf{A}(c)$  describes the lattice motif of  $\text{LiFePO}_4$  (red box). For  $0 < c < 1$ , intermediate lattice geometries of the interphase  $\text{Li}_x\text{FePO}_4$  (dashed black box) are modeled.

and  $\text{LiFePO}_4$  lattices and are obtained from Table I. At  $c = 0$ , the transformation coefficients in  $\mathbf{A}(c = 0)$ , Eq. (A4), represent the rectangular geometry of  $\text{FePO}_4$  in two dimensions [41] (see Fig. 6). For  $c = 1$  the transformation coefficients in  $\mathbf{A}(c = 1)$ , Eq. (A4), represent the rectangular geometry of  $\text{LiFePO}_4$ . Across the diffuse phase boundary,  $0 < c < 1$ , the transformation coefficients in  $\mathbf{A}(c(\bar{x}))$  are linearly interpolated and describe intermediate lattice geometries (see Fig. 6). This diffuse interface represents the coarse-grained lattice symmetry of the staging structure observed in  $\text{LiFePO}_4$  experiments [44].

We assume an isotropic bulk-diffusion coefficient  $D$  in Eq. (2) to model the evolution of the composition field as

$$\begin{aligned} \frac{\partial c}{\partial \tau} &= \nabla^2 \frac{\delta \mathcal{F}}{\delta c} \\ &= \nabla^2 \left( \frac{\partial g(c)}{\partial c} - \nabla^2 c + \gamma \frac{\psi}{2} \frac{\partial (\nabla_c^4 + 2\nabla_c^2) \psi}{\partial c} \right). \end{aligned} \quad (\text{A5})$$

Here,  $\tau$  is the dimensionless time variable  $\tau = t \frac{D}{L^2}$  and  $L$  is the size of the computation grid. Equation (8) introduces two Laplace operators,  $\nabla^2$  and  $\nabla_c^2$ , respectively. The Laplacian  $\nabla^2 = \frac{\partial^2}{\partial x^2} + \frac{\partial^2}{\partial y^2}$  describes an isotropic Li intercalation. We do, however, see anisotropy in Li intercalation arising from the coordinate-transformation coefficients in  $\nabla_c^2$  and from the presence of grain boundaries in the electrode. The coupled term  $\nabla^2 \gamma \frac{\psi}{2} \frac{\partial G(\nabla_c^2) \psi}{\partial c}$  is anisotropic and influences Li intercalation. This anisotropic contribution is negligible because of the diffuse width (approximately four coarse-grained lattices) of the phase boundary. Furthermore, the value of the constant  $\gamma$  also influences the anisotropy contribution from this coupled term. In this paper we set  $\gamma = \frac{\lambda^2 q_0^5}{u F_0} = 1$  for computational expediency. That is, the energy contribution from the PFC equation is negligible (i.e.,  $\sim 10^{-19} F_0$ ). Consequently, Li intercalation into electrodes is relatively unaffected by the anisotropy in  $\psi_{ij}$ . However, if  $\gamma$  is large, the effects from material crystallography and lattice defects are expected to appear in the simulation.

The lattice arrangement at each composition evolution step is computed as

$$\begin{aligned} \frac{\partial \psi}{\partial n} &= -\frac{\delta \mathcal{F}}{\delta \psi} + \frac{1}{L^2} \int \frac{\delta \mathcal{F}}{\delta \psi} d\bar{x} \\ &= -\gamma[(r + (1 + \nabla_c^2)^2)\psi + \psi^3] \\ &\quad + \frac{1}{L^2} \int \gamma[(r + (1 + \nabla_c^2)^2)\psi + \psi^3] d\bar{x}. \quad (\text{A6}) \end{aligned}$$

Here, we assume that the elastic relaxation (equilibrating the peak density field) is infinitely faster than the evolution of the composition field. Consequently, we model the equilibrium lattice arrangements by maintaining  $\frac{\delta \mathcal{F}}{\delta \psi} \approx 0$  throughout the phase transition. In Eq. (A6),  $n$  is a fictive timelike variable

that is rapidly changing in comparison to the dimensionless time,  $\tau$ . Further details on Eqs. (A1) and (A2) can be found in Ref. [34].

## 2. Modeling lattice symmetries using PFC methods

The coordinate transformation coefficients introduced in the CH-PFC model [34] resemble the lattice stretch and shear factors used in the anisotropic PFC methods [62,63]. The stretch/shear factors deform a lattice symmetry and are used to calculate the anisotropic model coefficients. The transformation coefficients in the CH-PFC model, however, differ from the anisotropic coefficients in that they are coupled to a composition field, which influences the underlying lattice symmetry of the host material.

- 
- [1] H. Van Swygenhoven, Grain boundaries and dislocations, *Science* **296**, 66 (2002).
- [2] M. Guttman, Grain boundary segregation, two dimensional compound formation, and precipitation, *Metall. Trans. A* **8**, 1383 (1977).
- [3] F. P. Knudsen, Dependence of mechanical strength of brittle polycrystalline specimens on porosity and grain size, *J. Am. Ceram. Soc.* **42**, 376 (1959).
- [4] A. Sharafi, C. G. Haslam, R. D. Kerns, J. Wolfenstine, and J. Sakamoto, Controlling and correlating the effect of grain size with the mechanical and electrochemical properties of  $\text{Li}_7\text{La}_3\text{Zr}_2\text{O}_{12}$  solid-state electrolyte, *J. Mater. Chem. A* **5**, 21491 (2017).
- [5] J. W. Martin, R. D. Doherty, and B. Cantor, *Stability of Microstructure in Metallic Systems* (Cambridge University Press, Cambridge, UK, 1997).
- [6] T. Watanabe, Grain boundary design and control for high temperature materials, *Mater. Sci. Eng. A* **166**, 11 (1993).
- [7] C. Handwerker, in *Diffusion Phenomena in Thin Films and Microelectronic Materials*, edited by D. Gupta and P. S. Ho (Noyes, Park Ridge, NJ, 1989), pp. 245–322.
- [8] M. Hillert and G. R. Purdy, Chemically induced grain boundary migration, *Acta Metall.* **26**, 333 (1978).
- [9] W. C. Carter and C. A. Handwerker, Morphology of grain growth in response to diffusion induced elastic stresses: Cubic systems, *Acta Metall. Mater.* **41**, 1633 (1993).
- [10] C. A. Handwerker and J. W. Cahn, Microstructural control through diffusion-induced grain boundary migration, *MRS Online Proc. Library Arch.* **106**, 127 (1987).
- [11] C. K. Christensen, M. A. H. Mamakhel, A. R. Balakrishna, B. B. Iversen, Y.-M. Chiang, and D. B. Ravnsbæk, Order-disorder transition in nano-rutile  $\text{TiO}_2$  anodes: A high capacity low-volume change Li-ion battery material, *Nanoscale* (2019), doi: 10.1039/C9NR01228A.
- [12] K. Xiang, W. Xing, D. B. Ravnsbæk, L. Hong, M. Tang, Z. Li, K. M. Wiaderek, O. J. Borkiewicz, K. W. Chapman, P. J. Chupas, and Y. M. Chiang, Accommodating high transformation strains in battery electrodes via the formation of nanoscale intermediate phases: Operando investigation of olivine  $\text{NaFePO}_4$ , *Nano Lett.* **17**, 1696 (2017).
- [13] G. Bucci, B. Talamini, A. R. Balakrishna, Y. M. Chiang, and W. C. Carter, Mechanical instability of electrode-electrolyte interfaces in solid-state batteries, *Phys. Rev. Mater.* **2**, 105407 (2018).
- [14] Y. Hu, X. Zhao, and Z. Suo, Averting cracks caused by insertion reaction in lithium-ion batteries, *J. Mater. Res.* **25**, 1007 (2010).
- [15] J. W. Cahn, P. Fife, and O. Penrose, A phase-field model for diffusion-induced grain-boundary motion, *Acta Mater.* **45**, 4397 (1997).
- [16] J. E. Taylor, J. W. Cahn, and C. A. Handwerker, Overview No. 98 I—Geometric models of crystal growth, *Acta Metall. Mater.* **40**, 1443 (1992).
- [17] K. Deckelnick, C. M. Elliott, and V. Styles, Numerical diffusion-induced grain boundary motion, *Interfaces Free Bound.* **3**, 393 (2001).
- [18] P. C. Fife, J. W. Cahn, and C. M. Elliott, A free-boundary model for diffusion-induced grain boundary motion, *Interfaces Free Bound.* **3**, 291 (2001).
- [19] M. Tang, W. C. Carter, and R. M. Cannon, Diffuse interface model for structural transitions of grain boundaries, *Phys. Rev. B* **73**, 024102 (2006).
- [20] Y. Mo, S. P. Ong, and G. Ceder, First principles study of the  $\text{Li}_{10}\text{GeP}_2\text{S}_{12}$  lithium super ionic conductor material, *Chem. Mater.* **24**, 15 (2011).
- [21] C. A. Fisher and M. S. Islam, Surface structures and crystal morphologies of  $\text{LiFePO}_4$ : Relevance to electrochemical behavior, *J. Mater. Chem.* **18**, 1209 (2008).
- [22] P. Bai, D. A. Cogswell, and M. Z. Bazant, Suppression of phase separation in  $\text{LiFePO}_4$  nanoparticles during battery discharge, *Nano Lett.* **11**, 4890 (2011).
- [23] H. Moriwake, A. Kuwabara, C. A. Fisher, R. Huang, T. Hitosugi, Y. H. Ikuhara, H. Oki, and Y. Ikuhara, First-principles calculations of lithium-ion migration at a coherent grain boundary in a cathode material,  $\text{LiCoO}_2$ , *Adv. Mater.* **25**, 618 (2013).
- [24] B. L. DeCost and E. A. Holm, Phenomenology of abnormal grain growth in systems with nonuniform grain boundary mobility, *Metall. Mater. Trans. A* **48**, 2771 (2017).
- [25] N. Meethong, H. Y. S. Huang, W. C. Carter, and Y. M. Chiang, Size-dependent lithium miscibility gap in nanoscale  $\text{Li}_{1-x}\text{FePO}_4$ , *Electrochem. Solid State Lett.* **10**, A134 (2007).
- [26] A. R. Balakrishna, J. E. Huber, and I. Münch, Nanoscale periodic domain patterns in tetragonal ferroelectrics: A phase-field study, *Phys. Rev. B* **93**, 174120 (2016).

- [27] I. Muench, A. R. Balakrishna, and J. E. Huber, Periodic boundary conditions for the simulation of 3D domain patterns in tetragonal ferroelectric material, *Arch. Appl. Mech.* **89**, 955 (2019).
- [28] J. A. Warren, R. Kobayashi, A. E. Lobkovsky, and W. C. Carter, Extending phase field models of solidification to polycrystalline materials, *Acta Mater.* **51**, 6035 (2003).
- [29] J. Yang and J. S. Tse, Li ion diffusion mechanisms in  $\text{LiFePO}_4$ : An ab initio molecular dynamics study, *J. Phys. Chem. A* **115**, 13045 (2011).
- [30] P. Zhang, Y. Wu, D. Zhang, Q. Xu, J. Liu, X. Ren, Z. Luo, M. Wang, and W. Hong, Molecular dynamics study on ion diffusion in  $\text{LiFePO}_4$  olivine materials, *J. Phys. Chem. A* **112**, 5406 (2008).
- [31] J. Zhao, A. Buldum, J. Han, and J. P. Lu, First-Principles Study of Li-Intercalated Carbon Nanotube Ropes, *Phys. Rev. Lett.* **85**, 1706 (2000).
- [32] A. F. Voter, F. Montalenti, and T. C. Germann, Extending the time scale in atomistic simulation of materials, *Annu. Rev. Mater. Res.* **32**, 321 (2002).
- [33] F. Montalenti and A. F. Voter, Applying accelerated molecular dynamics to crystal growth, *Phys. Status Solidi B* **226**, 21 (2001).
- [34] A. R. Balakrishna and W. C. Carter, Combining phase-field crystal methods with a Cahn-Hilliard model for binary alloys, *Phys. Rev. E* **97**, 043304 (2018).
- [35] K. R. Elder and M. Grant, Modeling elastic and plastic deformations in nonequilibrium processing using phase field crystals, *Phys. Rev. E* **70**, 051605 (2004).
- [36] M. Hillert and L. I. Staffansson, Regular-solution model for stoichiometric phases and ionic melts, *Acta Chem. Scand.* **24**, 3618 (1970).
- [37] M. Huttin and M. Kamlah, Phase-field modeling of stress generation in electrode particles of lithium ion batteries, *Appl. Phys. Lett.* **101**, 133902 (2012).
- [38] M. Tang, H. Y. Huang, N. Meethong, Y. H. Kao, W. C. Carter, and Y. M. Chiang, Model for the particle size, overpotential, and strain dependence of phase transition pathways in storage electrodes: Application to nanoscale olivines, *Chem. Mater.* **21**, 1557 (2009).
- [39] D. A. Cogswell and M. Z. Bazant, Coherency strain and the kinetics of phase separation in  $\text{LiFePO}_4$  nanoparticles, *ACS Nano* **6**, 2215 (2012).
- [40] A. Nakamura, S. Furutsuki, S. I. Nishimura, T. Tohei, Y. Sato, N. Shibata, A. Yamada, and Y. Ikuhara, Phase boundary structure of  $\text{Li}_x\text{FePO}_4$  cathode material revealed by atomic-resolution scanning transmission electron microscopy, *Chem. Mater.* **26**, 6178 (2014).
- [41] A. K. Padhi, K. S. Nanjundaswamy, and J. B. Goodenough, Phospho-olivines as positive-electrode materials for rechargeable lithium batteries, *J. Electrochem. Soc.* **144**, 1188 (1997).
- [42] H. Emmerich, H. Löwen, R. Wittkowski, T. Gruhn, G. I. Tóth, G. Tegze, and L. Gránásky, Phase-field-crystal models for condensed matter dynamics on atomic length and diffusive time scales: An overview, *Adv. Phys.* **61**, 665 (2012).
- [43] N. Ofori-Opoku, V. Fallah, M. Greenwood, S. Esmaili, and N. Provatas, Multicomponent phase-field crystal model for structural transformations in metal alloys, *Phys. Rev. B* **87**, 134105 (2013).
- [44] C. Zhu, L. Gu, L. Suo, J. Popovic, H. Li, Y. Ikuhara, and J. Maier, Size-dependent staging and phase transition in  $\text{LiFePO}_4/\text{FePO}_4$ , *Adv. Funct. Mater.* **24**, 312 (2014).
- [45] J. W. Cahn, Critical point wetting, *J. Chem. Phys.* **66**, 3667 (1977).
- [46] M. Tang, W. C. Carter, J. F. Belak, and Y. M. Chiang, Modeling the competing phase transition pathways in nanoscale olivine electrodes, *Electrochim. Acta* **56**, 969 (2010).
- [47] N. Provatas, J. A. Dantzig, B. Athreya, P. Chan, P. Stefanovic, N. Goldenfeld, and K. R. Elder, Using the phase-field crystal method in the multi-scale modeling of microstructure evolution, *JOM* **59**, 83 (2007).
- [48] M. Winning, G. Gottstein, and L. S. Shvindlerman, On the mechanisms of grain boundary migration, *Acta Mater.* **50**, 353 (2002).
- [49] K. G. F. Janssens, D. Raabe, E. Kozeschnik, M. A. Miodownik, and B. Nestler, *Computational Materials Engineering: An Introduction to Microstructure Evolution* (Academic Press, San Diego, CA, 2010).
- [50] D. Morgan, A. Van der Ven, and G. Ceder, Li conductivity in  $\text{Li}_x\text{MPO}_4$  ( $M = \text{Mn, Fe, Co, Ni}$ ) olivine materials, *Electrochem. Solid State Lett.* **7**, A30 (2004).
- [51] D. A. Cogswell and M. Z. Bazant, Size-dependent phase morphologies in  $\text{NaFePO}_4$  battery particles, *Electrochem. Commun.* **95**, 33 (2018).
- [52] G. Gottstein, A. H. King, and L. S. Shvindlerman, The effect of triple-junction drag on grain growth, *Acta Mater.* **48**, 397 (2000).
- [53] G. Gottstein and L. S. Shvindlerman, *Grain Boundary Migration in Metals: Thermodynamics, Kinetics, Applications* (CRC Press, Boca Raton, FL, 2009).
- [54] N. Balke, S. Jesse, A. N. Morozovska, E. Eliseev, D. W. Chung, Y. Kim, L. Adamczyk, R. E. Garcia, N. Dudney, and S. V. Kalinin, Nanoscale mapping of ion diffusion in a lithium-ion battery cathode, *Nat. Nanotech.* **5**, 749 (2010).
- [55] A. Ulvestad, A. Singer, J. N. Clark, H. M. Cho, J. W. Kim, R. Harder, J. Maser, Y. S. Meng, and O. G. Shpyrko, Topological defect dynamics in operando battery nanoparticles, *Science* **348**, 1344 (2015).
- [56] T. C. Narayan, F. Hayee, A. Baldi, A. L. Koh, R. Sinclair, and J. A. Dionne, Direct visualization of hydrogen absorption dynamics in individual palladium nanoparticles, *Nat. Commun.* **8**, 14020 (2017).
- [57] J. G. Swallow, W. H. Woodford, F. P. McGrogan, N. Ferralis, Y. M. Chiang, and K. J. Van Vliet, Effect of electrochemical charging on elastoplastic properties and fracture toughness of  $\text{Li}_x\text{CoO}_2$ , *J. Electrochem. Soc.* **161**, F3084 (2014).
- [58] W. H. Woodford, W. C. Carter, and Y. M. Chiang, Design criteria for electrochemical shock resistant battery electrodes, *Energy Environ. Sci.* **5**, 8014 (2012).
- [59] J. B. Bates, N. J. Dudney, B. Neudecker, A. Ueda, and C. D. Evans, Thin-film lithium and lithium-ion batteries, *Solid State Ion.* **135**, 33 (2000).
- [60] S. W. Kim, S. G. Kim, J. I. Jung, S. J. L. Kang, and I. W. Chen, Enhanced grain boundary mobility in yttria-stabilized

- cubic zirconia under an electric current, *J. Am. Ceram. Soc.* **94**, 4231 (2011).
- [61] Y. Dong, H. Wang, and I. W. Chen, Electrical and hydrogen reduction enhances kinetics in doped zirconia and ceria: I. Grain growth study, *J. Am. Ceram. Soc.* **100**, 876 (2017).
- [62] J. Kundin and M. A. Choudhary, Application of the anisotropic phase-field crystal model to investigate the lattice systems of different anisotropic parameters and orientations, *Model. Simul. Mater. Sci. Eng.* **25**, 055004 (2017).
- [63] R. Prieler, J. Hubert, D. Li, B. Verleye, R. Haberkern, and H. Emmerich, An anisotropic phase-field crystal model for heterogeneous nucleation of ellipsoidal colloids, *J. Phys.: Condens. Matter* **21**, 464110 (2009).